mater.scichina.com link.springer.com

Published online 18 November 2022 | https://doi.org/10.1007/s40843-022-2236-8
Sci China Mater 2023, 66(3): 1013–1023

Bifunctional Nb-N-C atomic catalyst for aqueous Zn-air battery driving CO_2 electrolysis

Sanshuang Gao[1], Tianwei Wang[1,2], Mengmeng Jin[1], Shusheng Zhang[3], Qian Liu[4], Guangzhi Hu[5*], Hui Yang[1], Jun Luo[1,6*] and Xijun Liu[2*]

ABSTRACT **Designing efficient and cost-effective bifunctional catalysts is desirable for carbon dioxide and oxygen reduction reactions (CO_2RR and ORR) to address carbon neutralization and energy conversion. Herein, a bifunctional CO_2RR and ORR catalyst for aqueous Zn-air battery (ZAB) self-driving CO_2RR electrolysis is developed using atomically dispersed niobium anchored onto N-doped ordered mesoporous carbon (Nb-N-C). The Nb-N-C atomic catalyst demonstrates aqueous CO_2RR activity with CO Faradaic efficiency up to 90%, ORR activity with a half-wave potential of 0.84 V *vs.* reversible hydrogen electrode, and ZAB activity with a peak power density of 115.6 mW cm^{-2}, owing to the high Nb atom-utilization efficiency and ordered mesoporous structure. Furthermore, two-unit ZABs in series, serving as the power source for the self-powered CO_2 electrolysis system, continuously convert CO_2 to CO with average productivity of 3.75 μmol h^{-1} mg$_{cat}^{-1}$ during the first 10 h. Moreover, theoretical calculations exhibit that atomic Nb anchored to N-doped carbon can form Nb–N coordination bonds, effectively reducing the energy barriers of potential-determining *COOH for CO_2RR and *O formation for ORR.**

Keywords: bifunctional catalyst, carbon dioxide reduction reaction, oxygen reduction reaction, Zn-air battery, self-powered CO_2 electrolysis

INTRODUCTION

The electrochemical CO_2 and O_2 reduction reactions (CO_2RR and ORR) are two fundamental reactions for CO_2 capturing and renewable energy supplying, which not only address global warming and energy crises but also enable the generation of valuable products [1–5]. However, designing multifunctional electrocatalysts for supplying renewable electricity and simultaneously converting CO_2 to value-added products (such as CO, HCOOH, C_2H_4, and CH_4) is still a significant challenge [6–13]. Generally, designing efficient and economically viable bifunctional electrocatalysts is regarded as a promising method for integrating CO_2RR and ORR activities [14,15]. Tremendous efforts have been devoted to developing efficient and cost-effective bifunctional catalysts, such as P, N co-coordinated fullerene-like carbons, Fe, N-co-doped bamboo-like carbon nanotubes, N-doped ordered mesoporous carbons (NOMC), biomass-derived carbon frameworks, and N, S co-doped hierarchically porous carbon (NSHPC) [16–20].

Prior investigations have illustrated that N-doped carbon (NC) matrix materials are widely used as substrates for loading major active sites due to their large specific surface area and preferable electrical conductivity [21–26]. According to our previous reports, metal-free NOMC displayed superior selectivity and stability for CO_2RR, revealing that NOMC is capable of enhancing CO_2RR performance [27]. Furthermore, NOMC exhibits a unique ordered mesoporous feature that enables uniform distribution of the active sites for catalyzing ORR [28–30]. The CO_2RR and ORR rates are dependent on the CO_2 and O_2 concentrations, which can be enhanced by increasing the CO_2 and O_2 transport to the electrode. It is suggested that ordered mesoporous structures can improve CO_2 and O_2 transport rates by increasing the gas permeability and effective diffusivity [26,27]. Generally, active centers anchored onto mesoporous carbon should be minimized in size (for instance, single-atoms or clusters) to maximize the utilization of the superficial area of the NC substrate [31–37]. Many pioneering efforts have also demonstrated that atomically dispersed active sites anchored onto NC substrates can effectively enhance ORR performances, indicating a preferable application of NC substrates [38–44], for instance, isolated single-atom Fe anchored on N-doped porous carbon and Cu-Zn clusters on porous NC [45–47]. Furthermore, transition metal-nitrogen-carbon (TM-N-C)-based catalysts have attracted widespread interest for CO_2RR electrocatalysis because their 3d electron orbitals endow metal-N_x (x denotes N coordination number) sites with efficient intrinsic CO_2RR activity [48–50]. Therefore, the rational design of bifunctional electrocatalysts containing dual-core active sites

[1] Institute for New Energy Materials and Low-Carbon Technologies, Tianjin Key Lab for Photoelectric Materials & Devices, School of Materials Science and Engineering, Tianjin University of Technology, Tianjin 300384, China
[2] MOE Key Laboratory of New Processing Technology for Non-Ferrous Metals and Materials, and Guangxi Key Laboratory of Processing for Non-Ferrous Metals and Featured Materials, School of Resource, Environments and Materials, Guangxi University, Nanning 530004, China
[3] College of Chemistry, Zhengzhou University, Zhengzhou 450000, China
[4] Institute for Advanced Study, Chengdu University, Chengdu 610106, China
[5] Institute for Ecological Research and Pollution Control of Plateau Lakes School of Ecology and Environmental Science, Yunnan University, Kunming 650504, China
[6] Shenzhen Institute for Advanced Study, University of Electronic Science and Technology of China, Shenzhen 518110, China
* Corresponding authors (emails: jluo@uestc.edu.cn (Luo J); guangzhihu@ynu.edu.cn (Hu G); xjliu@tjut.edu.cn (Liu X))

for both CO_2RR and ORR has significant practical applications. Although Nb single atoms loading to graphitic layers, Nb-based binary nitride materials doping with Co and Nb_4N_5 nanoparticles have been reported to overcome the sluggish kinetics of ORR and CO_2RR [51–53]. Atomically dispersed Nb on NC substrates has rarely been used in bifunctional catalysts.

Motivated by the aforementioned discoveries, herein, atomically dispersed Nb anchored onto N-doped ordered mesoporous carbon (Nb-N-C) electrocatalyst was designed for independent dual-core active sites, where Nb-N-C served as CO_2RR/ORR active sites. Atomically dispersed Nb atoms were uniformly distributed around carbon nanopores, which was beneficial for capturing and transferring CO_2 or O_2 molecules [54]. The Nb-N-C catalyst demonstrated a CO Faradaic efficiency (FE) of up to 90% for aqueous CO_2RR activity and a half-wave potential ($E_{1/2}$) of 0.84 V *vs*. reversible hydrogen electrode (RHE) for ORR activity, which was higher than that of NC and 20 wt% Pt/C counterparts. Theoretical calculations also exhibited that the Nb-N-C structure has reduced the Gibbs free energy (ΔG) of *COOH for CO_2RR and *O formation for ORR, revealing that atomically dispersed Nb atoms are responsible for the CO_2RR/ORR performance.

EXPERIMENTAL SECTION

Catalyst preparation

In a typical synthesis, an ordered mesoporous silica (SBA-15, 0.5 g) template, niobium chloride ($NbCl_5$, 0.32 g), and 4.0 mL ethanol were thoroughly mixed, and air dried. The as-obtained template was transferred to a 50-mL round-bottom flask containing ethylenediamine (EDA, 2.0 g) and carbon tetrachloride (CTC, 4.0 g) liquid mixture. The mixture precursor was ultrasonically dispersed for 5 min and then refluxed in an oil bath for 6 h until EDA and CTC polymerized completely. Subsequently, the post-polymerized brown precursor was carbonized at 900°C with a heating rate of 5°C min^{-1}. Finally, the carbon-based compound was etched for 12 h with 8 wt% hydrofluoric acid (HF) to remove the undesirable SBA-15 template. The Nb-N-C was successfully obtained by filtration with deionized water and dried at 80°C. Similarly, NC was synthesized in the same manner as Nb-N-C, but without the addition of the $NbCl_5$ reagent.

Electrochemical measurements

The ORR measurements were performed in a five-pool reactor with 0.1 mol L^{-1} KOH solution as the electrolyte, using a glassy carbon electrode (GCE, 5 mm in diameter), RHE, and carbon rod as the working, reference, and counter electrodes, respectively. Typically, the inks (e.g., Nb-N-C, NC, and Pt/C) were applied on GCE to form a loading of 0.3 mg cm^{-2}. The linear sweep voltammetry (LSV) was conducted in N_2/O_2-saturated conditions at 400–1600 r min^{-1}. The CO_2RR measurement processes were carried out as described in the literature [27]. For Zn-air battery (ZAB) measurements, the catalytic inks were dropped onto Ni foam to form a loading of 1.0 mg cm^{-2}. Subsequently, the moisture barrier was covered and pressed onto the Ni foam current collector, exposing a 0.63 cm^2 active area for attaching air. The LSV curves from 1.7 to 0 V were recorded to evaluate the power density performance, and the constant-current method was selected to investigate the discharge performance. All electrochemical measurements are detailed in the Supplementary information.

Catalyst characterization

Transmission electron microscopy (TEM), high-angle annular dark-field scanning TEM (HAADF-STEM), and energy dispersive X-ray spectroscopy (EDX) mapping of the samples were examined using JEM-ARM200F. The powder X-ray diffraction (XRD) pattern was recorded from 10° to 80°. Furthermore, X-ray photoelectron spectroscopy (XPS) spectra, the Fourier transform extended X-ray absorption fine structure (FT-EXAFS) of the Nb-N_4O model and X-ray absorption near edge structure (XANES) were conducted to identify the coordination environment of Nb-N-C, and N_2 adsorption-desorption isotherms were measured to characterize the internal structure and specific area.

RESULTS AND DISCUSSION

Characterizations

The detailed procedure of synthesizing Nb-N-C is schematized in Fig. 1a, where $NbCl_5$, EDA, and CTC act as the sources for Nb, nitrogen, and carbon, respectively. All of the aforementioned precursors ultimately filled the ordered pores of the SBA-15 template. As depicted in Figs S1 and S2a, b, abundant Nb-N-C and NC fibers possess similar diameters with an average of 150 nm and an intertwined string-like morphology, which may be caused by rotating magneton forces from the ordered agglomeration of SBA-15 templates. The TEM images of Nb-N-C and NC are depicted in Fig. 1b and Fig. S2c, d, and the ordered arrangement of pore channels in Nb-N-C and NC fibers confirm the morphology structure of SBA-15 templates. It is worth noting that the average pore sizes for Nb-N-C and NC fibers are 5 and 6 nm, respectively, which is consistent with the Brunauer-Emmett-Teller (BET) pore size distribution results. The NC exhibits a specific surface area of 747.2 m^2 g^{-1}, slightly greater than the 741.4 m^2 g^{-1} of Nb-N-C fibers (Fig. S3); this is attributable to the fact that both NC and Nb-N-C employ the same SBA-15 templates as the pore-forming substances.

Furthermore, the XRD patterns of Nb-N-C and NC revealed that no obvious crystalline Nb metal was present (Fig. S4). From HAADF-STEM images, numerous randomly distributed Nb atoms have been assembled into ultrathin clusters (Fig. 1d). The co-existence of Nb single atoms, clusters (in white circles), and ultrasmall pores (in irregular red circles) confirmed the porous structure of Nb-N-C fibers, as depicted in Fig. 1c–e. EDX mappings of Nb-N-C and NC are displayed in Fig. 1f, where C, N, O, and Nb are uniformly incorporated into the Nb-N-C. In contrast, the weak signal of the Nb element is probably attributable to the absence of Nb-related precursors during the NC synthesis. The 1.27 wt% Nb content was calculated using inductively coupled plasma mass spectrometry (ICP-MS) based on the standard curve of Nb.

XPS analysis reveals that Nb atoms with oxidation valence state have been successfully incorporated into the NC matrix, as illustrated in Fig. 2a and Fig. S5a, which is consistent with the EDX mapping results (Fig. 1f). The binding energy peaks of Nb 3d spectra emerged at 205.5, 207.2, and 209.9 eV, corresponding to Nb^{5+}-$N_{5/2}$, Nb^{5+}-$O_{5/2}$, and Nb^{5+}-$O_{3/2}$, respectively [53,55]. On the contrary, no distinguishable Nb-related signals can be observed for NC. The O 1s and N 1s spectra located at approximately 397.4 and 530.4 eV, respectively, could also be fitted with two peaks of Nb–N and Nb–O (Fig. S5b, c), corresponding to the results depicted in Fig. 2a [56,57]. The com-

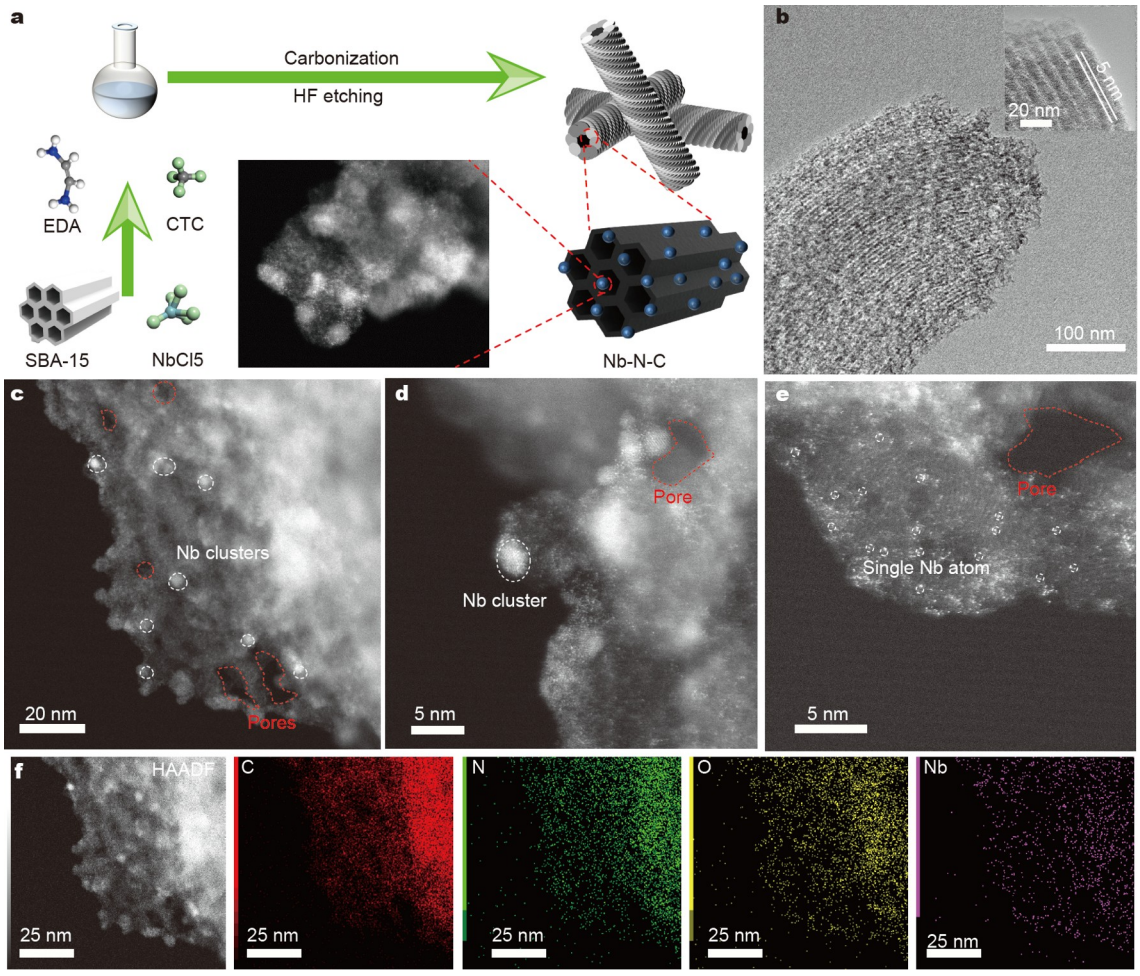

Figure 1 Synthesis strategy (a) and characterizations (b–f) of Nb-N-C. (b) Low-resolution and inserted high-resolution TEM images, (c–e) HAADF-STEM images of different resolutions, and (f) HAADF-STEM and EDX mappings of C, N, O, and Nb.

parison of C 1s spectra demonstrated the absence of Nb–C bonds in Nb-N-C (Fig. S5d).

The FT-EXAFS and XANES were measured to identify the coordination environment of Nb-N-C to confirm the coordination situation of Nb [58]. As demonstrated in Nb K-edge XANES profiles (Fig. 2b), the absorption intensity of Nb-N-C is stronger than that of Nb foil, which anastomoses the oxidation valence state of Nb species and is consistent with the XPS results in Fig. 2a. The FT-EXAFS of Nb-N-C in Fig. 2c reveals that the Nb–N coordination shell peaks at approximately 1.53 Å, and no distinguishable Nb–Nb signals can be observed in Nb-N-C, indicating the existence of Nb–N coordination [59]. The EXAFS fitting curve (Fig. 2d) reveals that the Nb element was five-fold coordinated by four N atoms and one O atom (Nb-N_4O), which is significantly similar to the structure depicted in the inset. Both the EXAFS fitting curve and the FT-EXAFS results agree with the XPS results in Fig. 2a.

ORR performance

The ORR performance was evaluated using a three-electrode system, with 60 μg of catalyst loaded on a GCE (5 mm in diameter). Cyclic voltammetry (CV) curves of Nb-N-C were measured in N_2 or O_2-saturated 0.1 mol L^{-1} KOH solution to evaluate the ORR performance. As depicted in Fig. 3a, the O_2-saturated CV curve displays an obvious reduction peak at 0.71 V, demonstrating the outstanding activity of ORR. In contrast, the N_2-saturated CV curve exhibits a featureless current from 0.1 to 1.2 V. The LSV curves of Nb-N-C, Pt/C, and NC have been recorded at 1600 r min^{-1} and 10 mV s^{-1} in an O_2-saturated atmosphere to further compare the ORR performance. As depicted in Fig. 3b, c, the onset potential (E_{onset} = 0.91 V) and limiting diffusion current density (J = −4.6 mA cm^{-2}) of Nb-N-C are slightly lower than that of Pt/C (E_{onset} = 0.93 V, J = −5.7 mA cm^{-2}) and significantly higher than those of NC (E_{onset} = 0.82 V, J = −2.4 mA cm^{-2}), which correspond to the optimal Tafel slope of 94.6 mV dec^{-1} for Nb-N-C. Remarkably, Nb-N-C exhibits an $E_{1/2}$ potential of 0.84 V, which is 120 and 10 mV larger than those of NC and Pt/C catalysts and superior to the distorted Nb-doped graphene (N-Nb-G, $E_{1/2}$ = 0.82 V) in Table S1 [60]. These above-mentioned comparisons reveal that Nb-N-C exhibits excellent ORR catalytic activity, which is close to precious state-of-the-art Pt/C catalysts while also overcoming the sluggish kinetics of ORR.

The LSV curves were measured with rotating speeds (ω) ranging from 400 to 1600 r min^{-1} to better understand the mechanism of the ORR process. The J gradually increased with E_{onset} = 0.91 V for Nb-N-C and E_{onset} = 0.82 V for NC, as illustrated in Fig. 3d and Fig. S6a. According to the Koutecky-

Levich (K-L) plots, the J^{-1} is capable of fitting a line to $\omega^{-1/2}$, and the slope of Equation S2 can be utilized to calculate the number of transfer electrons. The current densities under different potentials (from 0.3 to 0.7 V) are fitted with $\omega^{-1/2}$ based on K-L plots, and the transfer electrons number of Nb-N-C was estimated to be 3.9–4.2, revealing the 4e⁻ process for Nb-N-C,

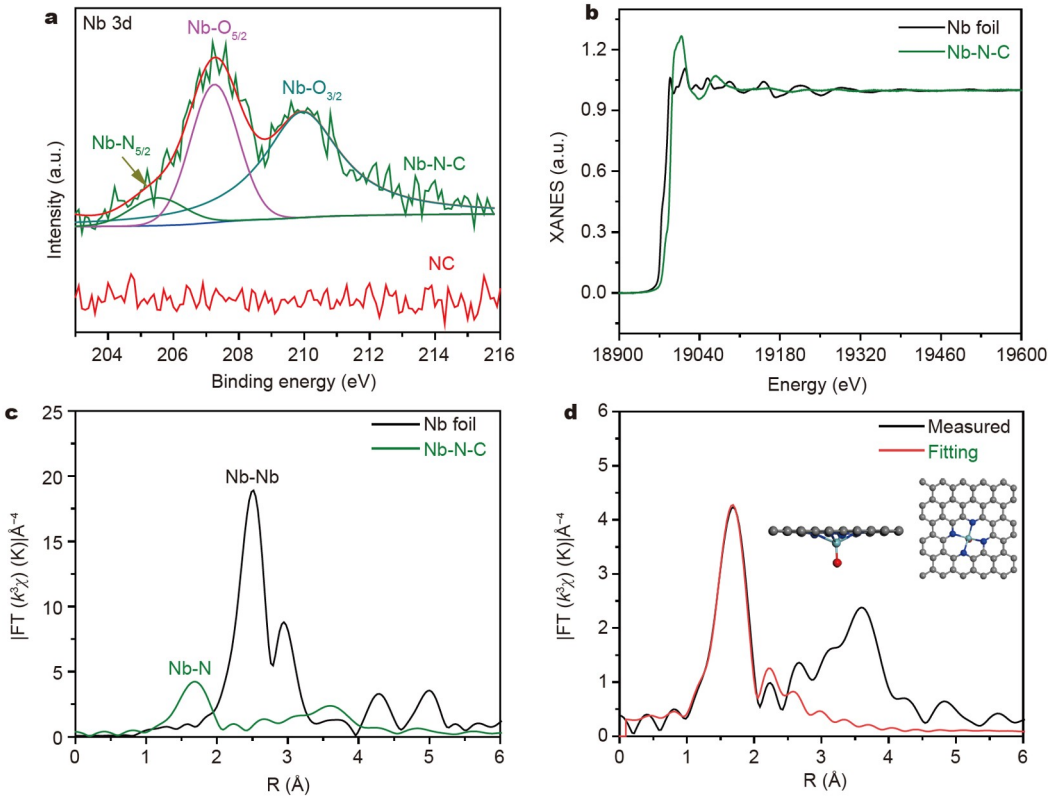

Figure 2 (a) High-resolution XPS of Nb 3d spectrum, (b) synchrotron radiation XANES characterization for Nb K-edge, (c) FT-EXAFS of Nb-N_4O in Nb-N-C, and (d) EXAFS fitting results in *R* space and the inserted Nb-N_4O structure diagram.

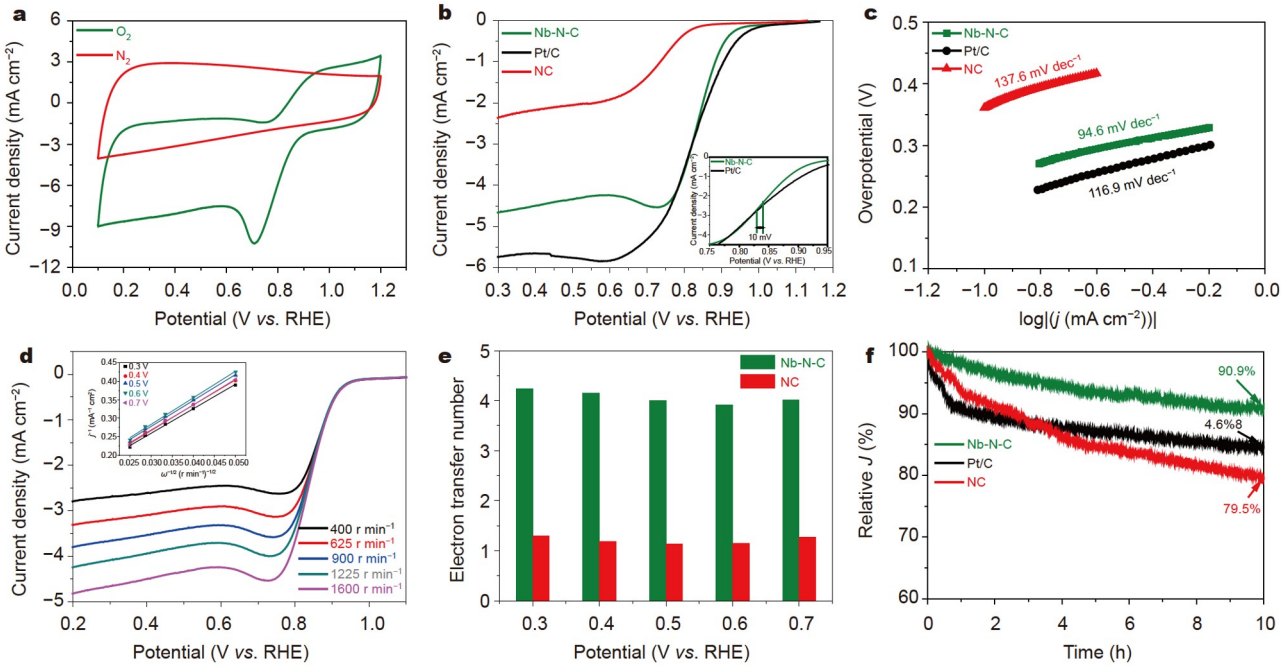

Figure 3 ORR electrocatalysis performance of the Nb-N-C sample. (a) CV curves of Nb-N-C ranging from 0.1 to 1.2 V under N_2 and O_2-saturated conditions in 0.1 mol L^{-1} KOH, (b) LSV curves of Nb-N-C, Pt/C, and NC with the overlap part enlarged, (c) comparison of the Tafel curves of Nb-N-C, Pt/C, and NC, (d) rotating rates of Nb-N-C from 400 to 1600 r min^{-1} with the calculated K-L plots of j^{-1} *vs.* $\omega^{-1/2}$ inserted, (e) calculated transfer electron numbers of Nb-N-C and NC, and (f) relative current densities of Nb-N-C, Pt/C, and NC.

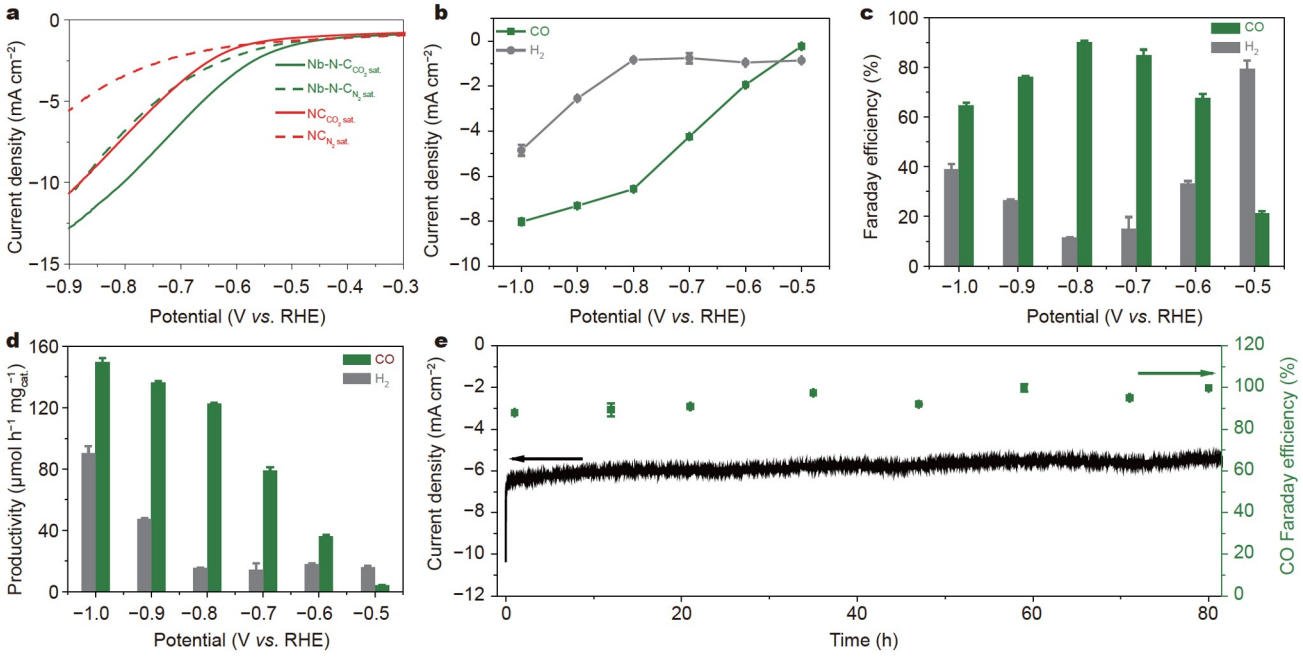

Figure 4 CO_2RR electrocatalysis performance of the Nb-N-C sample. (a) Polarization curves of Nb-N-C and NC ranging from 0.3 to 0.9 V under N_2 and O_2-saturated conditions in 0.1 mol L^{-1} $KHCO_3$, (b–d) j_{CO/H_2}, FE_{CO/H_2}, and CO/H_2 productivity at different reduction potentials, and (e) the 80-h CO_2RR durability measurement.

which could accelerate the sluggish kinetics for ORR (Fig. 3c, e). By contrast, NC only maintains the transfer electron numbers from 1.1 to 1.3, confirming the featureless current of NC for ORR (Fig. S6b). Chronoamperometric curves were recorded in an O_2-saturated atmosphere at 1600 r min^{-1} and 0.6 V, as illustrated in Fig. 3f. The relative current values deduced from these curves for evaluating the durability of Nb-N-C, Pt/C, and NC catalysts reveal that Nb-N-C exhibits the best ORR stability after the 10-h measurement, retaining a relative current of more than 90.9%, which is significantly higher than the values of 84.6% for Pt/C and 79.5% for NC. When compared with pioneering reports, Nb-N-C also displays outstanding $E_{1/2}$ and E_{onset} values. The electrochemical active area (ECSA) was characterized using the double-layer (C_{dl}) measurement, and EIS responded to the resistance of this system to develop a better comprehension of the superior ORR performance of the Nb-N-C catalyst. As depicted in Fig. S7, the CV of Nb-N-C (NC) was recorded at non-Faraday intervals with the scan rates ranging from 10 to 120 mV s^{-1}. Based on the comparison of the calculated C_{dl} (4.8 mF cm^{-2} for Nb-N-C and 2.4 mF cm^{-2} for NC), the Nb-N-C exhibits a double ECSA than that of NC, implying that a substantial surface area of NC is inactive toward ORR. Furthermore, Nb-N-C possesses half-circle impedance that is slightly smaller than that of NC, indicating that the Nb-N-C catalyst is able to reduce the interfacial charge-transfer resistance and accelerate the electrochemical reactions (Fig. S8).

CO_2RR performance

The CO_2RR activity was investigated in an H-cell, which contains the CO_2-saturated 0.1 mol L^{-1} $KHCO_3$ as the electrolyte. Typically, 1.0 mg catalyst was loaded on 1.0 cm^2 carbon paper (CP) to develop a working electrode. LSV curves of Nb-N-C and NC were measured at potentials ranging from −0.3 to −0.9 V under N_2 or CO_2-saturated conditions. As demonstrated in Fig. 4a, both currents of Nb-N-C and NC are higher under CO_2-saturated conditions than that under N_2-saturated conditions, implying that they exhibit preferable CO_2RR performance and simultaneously reveal that the total current density (j) of Nb-N-C is slightly higher than that of NC. Fig. 4b displays a comparison of partial current densities for CO and H_2 (j_{CO} and j_{H_2}). For the Nb-N-C catalyst, j_{H_2} remains constant and then rises sharply with the potential enhancement from −0.8 to −1.0 V, while the increased rate of j_{CO} drops sharply, which is consistent with the FE_{CO} and FE_{H_2} variation tendency displayed in Fig. 4c. The FE_{CO} increases from 21% to 90%, then decreases to 65%, confirming that FE_{H_2} fails from 79% to 11%, then increases to 39%.

The Nb-N-C catalyst exhibits the maximum CO selectivity at −0.8 V *vs.* RHE. Fig. 4d also displays the calculated CO and H_2 productivities; at a reductive potential of −1.0 V *vs.* RHE, CO productivity continuously rises to 149.7 μmol h^{-1} mg_{cat}^{-1}, while the H_2 productivity primarily retains a steady level before −0.8 V *vs.* RHE, and then increases to 90.5 μmol h^{-1} mg_{cat}^{-1}. The variation tendency of CO/H_2 productivity and j can be observed in Fig. S9; the higher negative potential facilitates the CO_2-to-CO/H_2O-to-H_2 processes, confirming the variation tendency of gas chromatography (GC) signals. When the chronoamperometric curve was utilized to evaluate the stability of CO_2RR exhibited in Fig. 4e, Nb-N-C exhibited outstanding stability for 80 h at the optimal reductive potential (−0.8 V *vs.* RHE) and achieved a current density of ~6.0 mA cm^{-2} and an FE_{CO} of ~90%, outperforming the selectivity of Pd-modified niobium nitride (Pd/NbN), Nb-doped MoS_2 catalyst ($Mo_{0.95}Nb_{0.05}S_2$), NSHPC and nitrogen-doped carbon nanotubes (NCNTs) listed in Table S2. Notably, the ordered mesoporous structure, Nb cluster/single

atom (in white circles), ultrasmall pores (in irregular red circles), and Nb element are distributed uniformly over the Nb-N-C catalyst after 80 h of CO_2RR electrocatalysis, manifesting the outstanding stability of Nb-N-C catalyst (Fig. S10). Moreover, no distinguishable signals were observed in the ^1H nuclear magnetic resonance (NMR) spectrum (Fig. S11), indicating that CO and H_2 are the major products for Nb-N-C. For the NC catalyst, the j_{H_2} remains stable and j_{CO} increases gradually (Fig. S12), yielding a maximum FE_{CO} of 93.6% and a CO productivity of 153.5 μmol h^{-1} mg_{cat}^{-1} (Fig. S13). Notably, the j_{CO} of NC before −0.8 V *vs.* RHE is less than that of Nb-N-C, revealing that the active sites of the Nb-N-C catalyst are more effective at the lower overpotential. The CO_2RR current density enhancement of Nb-N-C is attributed to the Nb-doping process, which increases the number of active sites while reducing the interfacial charge-transfer resistance. As illustrated in Fig. S14, the detected CO and H_2 signals of the NC catalyst gradually increase, anastomosing the results of Fig. S9, which demonstrate that the optimal FE_{CO} and CO productivity of NC are approximately similar to that of Nb-N-C results. Meanwhile, the NC catalyst has demonstrated CO_2RR performances similar to Nb-N-C, indicating that NC substrates can act as an alternative active core for catalyzing CO_2RR under high overpotentials.

ZAB performance

Motivated by the superior ORR performance, the Nb-N-C catalysts were designed to assemble a homemade ZAB. In the typical ZAB reaction, the zinc metal anode and air cathode are operated in an alkaline medium. During the discharge process, the zinc electrode dissolution drives the cathodic ORR (forward Reactions (1) and (2)) along with anodic Zn metal, which forms zincate ions ($Zn(OH)_4^{2-}$) and further decomposes into insoluble zinc oxide (ZnO). Conversely, during the charging process, oxygen and zinc metal regenerate (backward Reactions (1) and (2)). The reaction involved in a ZAB is illustrated as follows [61,62]:

$$\text{Anode: } Zn + 4OH^- \Leftrightarrow Zn(OH)_4^{2-} + 2e^-,\ E = -1.26\ V, \quad (1)$$

$$\text{Cathode: } O_2 + 2H_2O + 4e^- \Leftrightarrow 4OH^-,\ E = 0.4\ V, \quad (2)$$

$$\text{Overall reaction: } O_2 + 2Zn \Leftrightarrow 2ZnO,\ E = 1.66\ V. \quad (3)$$

As illustrated in Fig. 5a, Zn plate and Nb-N-C catalysts were utilized as the anodic fuel and cathodic catalyst, respectively, and are capable of causing Zn oxidation and ORR during the discharge process. Fig. 5b depicts the open-circuit voltage of 1.42 V for the Nb-N-C-based ZAB, identifying the value of the inserted multimeter photograph, which is slightly lower than that of Pt/C (1.46 V) and exceeds 0.03 V for the NC-based ZAB. The discharge polarization curves of ZABs based on Nb-N-C catalysts are shown in Fig. 5d, and when compared with the state-of-the-art Pt/C and NC catalysts, the Nb-N-C-based ZAB exhibits a maximum power density of 115.6 mW cm^{-2} at a discharge current density of 180 mA cm^{-2} and a voltage of 0.64 V, which are significantly higher than those for Pt/C- (104.7 mW cm^{-2}) and NC-based (78.3 mW cm^{-2}) ZABs. The preferable discharge property of Nb-N-C-based ZAB was employed to successfully drive the light-emitting diode (LED) displaying "Zn-air", verifying the practical application of the homemade ZAB (Fig. 5c).

The discharge properties of the Nb-N-C-, Pt/C-, and NC-based ZABs were investigated by enhancing the discharge current density from 10 to 100 mA cm^{-2} (Fig. 5e). Notably, both Nb-N-C- and Pt/C-based ZABs demonstrated stable discharge voltages in 10–100 mA cm^{-2}. Before 50 mA cm^{-2}, the discharge voltage of the Nb-N-C-based ZAB was slightly less than that of the Pt/C catalyst, but it increased with discharge current to surpass Pt/C, demonstrating that the Nb-N-C catalyst can be comparable to the Pt/C catalyst. Importantly, the discharge voltage of the Nb-N-C-based ZAB at 10 mA cm^{-2} is capable of backing to the primary potential, indicating excellent reproducibility. In contrast, the NC-based ZAB exhibits an unstable discharge platform and an undesirable discharge voltage, revealing the poor ZAB performance of NC. It is attributed to a lack of active sites for ORR catalysis.

The anode utilization and capacity of the Nb-N-C- and Pt/C-based ZABs were measured using prolonged discharge curves at 10 mA cm^{-2} (detailed calculations are provided in the Supplementary information). The Nb-N-C- and Pt/C-based ZABs display actual capacities of 685.75 and 762.04 mA h g^{-1}, respectively, and the calculated anode utilization is 83.1% for Nb-N-C and 92.4% for Pt/C, indicating that the Nb-N-C catalysts exhibit a comparable Zn plate consumption rate against Pt/C (Fig. 5g). The Zn anode in an alkaline environment would undergo a self-etching process and H_2 evolution reaction, which enables the consumption of some Zn metal, causing the anode utilization below 100% [63]. Since the hydrogen evolution reaction (HER) and ORR are competing reactions, which means that a better ORR performance will inhibit HER and cause preferable anode utilizations. The preferable ORR performance of Pt/C has caused superior anode utilization to that of the Nb-N-C. The rechargeability of ZABs assembled with IrO_2 and Nb-N-C (1:1 mass ratio) mixture was evaluated using a 20-min discharge and 20-min charge cycle at 10 mA cm^{-2} in an electrolyte of 6 mol L^{-1} KOH and 0.2 mol L^{-1} zinc acetate. As depicted in Fig. 5h, IrO_2 and Nb-N-C compounds were quite stable before the 80-h cyclic measurement with 48.5% voltampere efficiency (VE, ratio voltage platforms of discharging and charging) and then slightly decreased to 44.5% VE until 140 h, indicating only 4% VE attenuation during the prolonged cyclic measurement. However, when the same ratio of IrO_2 and Pt/C compound was loaded as its counterpart, it exhibited a significantly lower discharge voltage (0.86 V) and poor rechargeability within 24 h. The "Pt/C + IrO_2" catalyst exhibits obvious activity decay during the cycling, most probably due to the oxidation and loss of Pt metals under positive potentials [49,64].

ZAB-powered CO_2 electrolysis performance

Inspired by the excellent ZAB and CO_2RR performances of the Nb-N-C catalyst, the aforementioned homemade ZAB was utilized for self-powered CO_2 electrolysis, mimicking the self-powered H_2 product system [65]. As depicted in Fig. 6a, the ZAB and CO_2RR units were assembled with the Nb-N-C catalysts as the cathodes, which were connected in series to the Zn plate and carbon rod, respectively. The ZAB-powered CO_2 electrolysis system is illustrated in Fig. 6b, where two-unit ZABs (serving as the power source) and a single H-cell (serving as the CO_2RR device) are connected in series. As demonstrated in Fig. S15, two-unit ZABs in series display an open-circuit voltage of 2.83 V, indicating the double value of the single ZAB in Fig. 5b, and a single H-cell loaded with two-unit ZABs exhibits a voltage of 2.71 V. It is worth noting that this voltage alleviates the formation of bubbles, indicating a reductive reaction on the Nb-N-C electrode (see the Supplementary video).

The gaseous product of ZAB-powered CO_2 electrolysis was

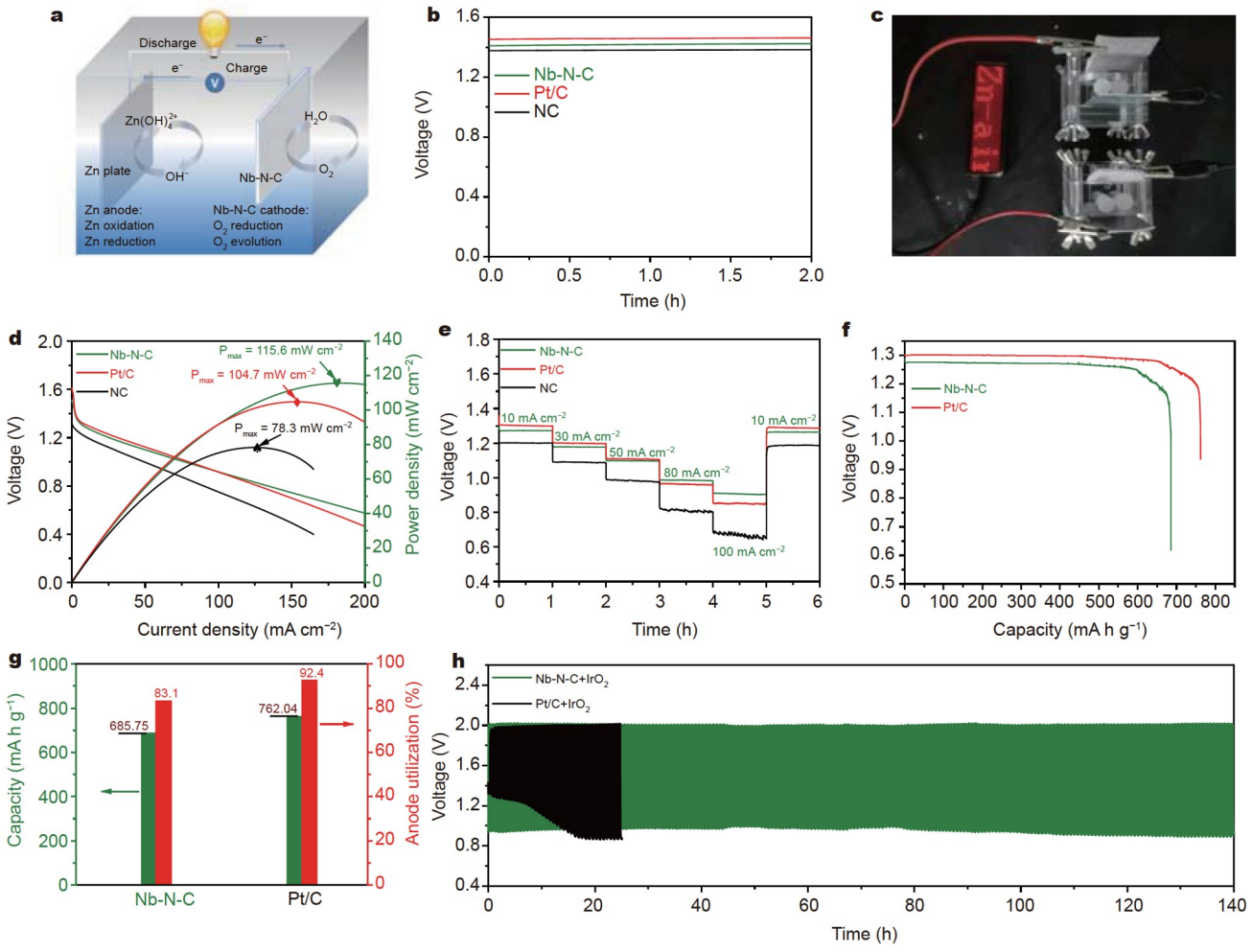

Figure 5 Schematic illustration of a ZAB (a) and the electrocatalysis performance of the ZABs (b–h). (b) Open-circuit voltages of ZABs assembled with Nb-N-C, Pt/C, and NC cathodes, (c) photograph of two serial batteries lighting up an LED, (d) comparison of Nb-N-C, Pt/C, and NC discharge polarization curves relating to power density, (e) 1-h discharge steps of ZABs using Nb-N-C, Pt/C, and NC cathodes in 10–100 mA cm^{-2}, (f) long-term discharge curves of Nb-N-C and Pt/C at the discharge current density of 10 mA cm^{-2} until the 0.1-mm anodic Zn plate breaks down, (g) capacity and anode utilization comparison of Nb-N-C and Pt/C calculated from Zn consumption, and (h) discharge/charge cycling curves of Nb-N-C/IrO_2 (mass ratio, 1:1) and Pt/C/IrO_2 (mass ratio, 1:1) mixtures at the discharge current density of 10 mA cm^{-2}.

detected by the thermal conductivity detector (TCD) of GC. As depicted in Fig. S16, the CO product signals peak around 8.3 min without observable H_2 product, verifying that only CO_2RR occurs on the Nb-N-C surface. Subsequently, the CO productivity was calculated using the volume fraction of GC, and the battery voltage was recorded during a 50-h stability test. The CO productivity maintains a steady level within 10 h (from 4.1 to 3.9 μmol h^{-1} mg_{cat}^{-1}) and then decreases slightly from 3.9 to 2.1 μmol h^{-1} mg_{cat}^{-1}, while the battery voltage remains unchanged during the entire process (Fig. 6c, d). The decrease in CO productivity is probably due to the anodic Zn plate's continuous consumption to form ZnO, which covers the surface of the Zn plate and inhibits the self-powered reduction [66]. The obtained results demonstrate the viability of ZAB-powered CO_2 electrolysis, which provides a novel strategy without any extra energy input for CO_2RR electrolysis.

Density functional theory (DFT) simulations

The intrinsic CO_2RR and ORR reactivity of NC and Nb-N-C catalysts were also evaluated using DFT calculations. According to the N 1s spectra of XPS and synchrotron radiation XANES fitting results (Fig. S5b and Fig. 2d), graphitic-N and Nb-N_4O were selected to simulate the bifunctional catalyst for catalyzing CO_2RR under U = 0/−0.8 V and ORR under U = 0/1.23 V, respectively [67–70]. The fundamental reaction mechanisms of the CO_2RR are as follows [65,71–80]:

$CO_2 + H^+ + e^- \rightarrow {}^*COOH$,

${}^*COOH + H^+ + e^- \rightarrow {}^*CO + H_2O$,

${}^*CO \rightarrow CO + {}^*$.

The ORR pathways are as follows [81–89]:

$O_2 + {}^* \rightarrow {}^*O_2$,

${}^*O_2 + H_2O + e^- \rightarrow {}^*OOH + OH^-$,

${}^*OOH + e^- \rightarrow {}^*O + OH^-$,

${}^*O + H_2O + e^- \rightarrow {}^*OH + OH^-$,

${}^*OH + e^- \rightarrow OH^- + {}^*$.

The coupled proton-electron transfer step occurs during the CO_2-to-CO transformation, as illustrated in Fig. 7a, determining the maximum uphill energy barrier of ${}^*COOH$ formation. Both graphitic-N sites in the NC and Nb-N_4O sites of Nb-N-C catalysts are preferred to reduce the uphill energy barrier of ${}^*COOH$

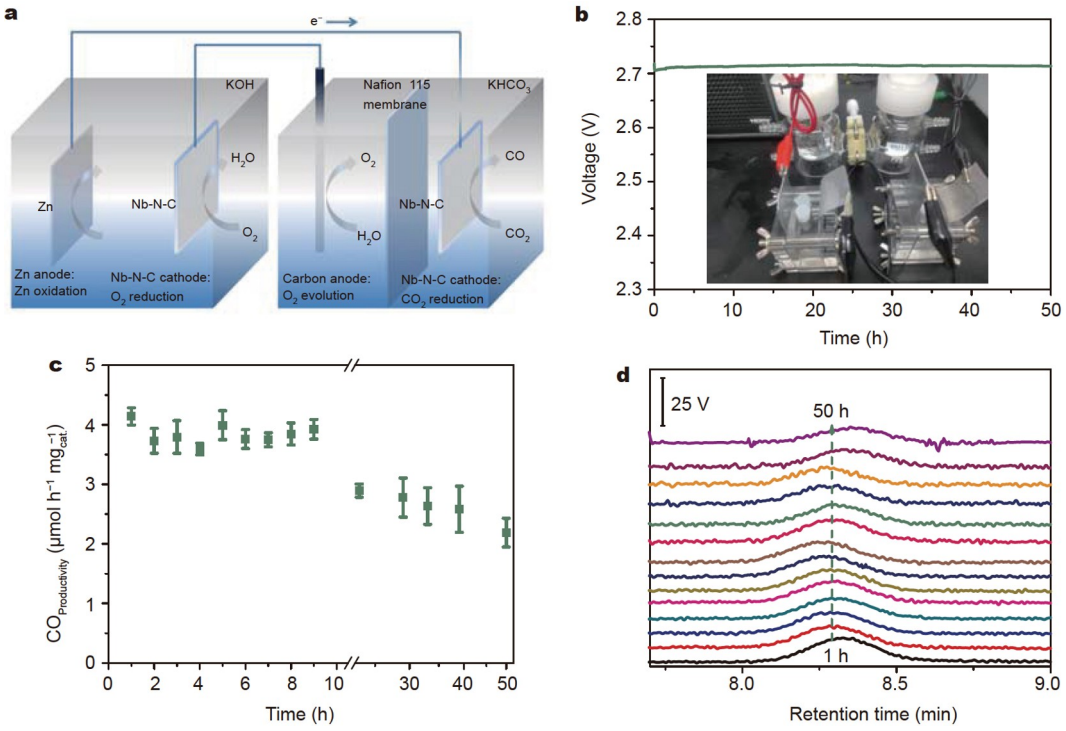

Figure 6 Schematic diagram of the homemade ZAB (a) and the ZAB-powered CO_2 electrolysis performance of Nb-N-C (b–d). (b) Voltages of two serial ZABs. Inset: the photograph of CO_2 electrolysis system. (c) CO productivity variation of 50-h continuous CO_2 electrolysis and (d) the corresponding GC signals.

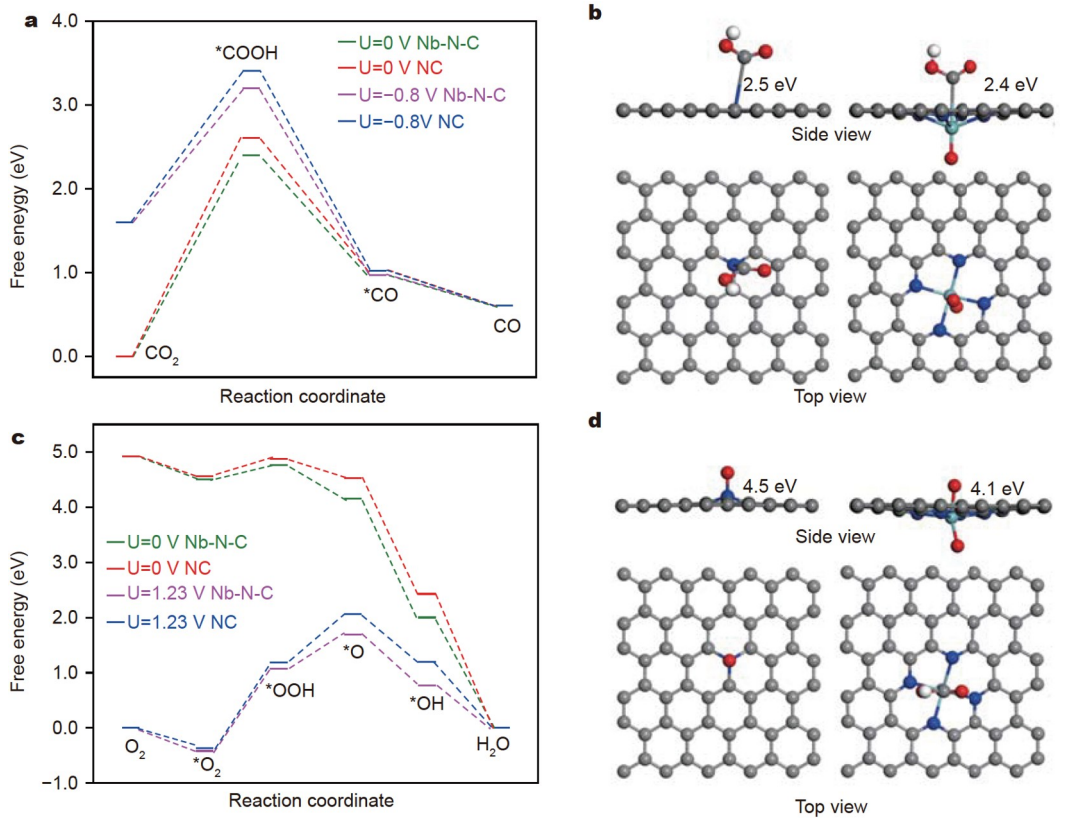

Figure 7 (a) Free-energies of NC and Nb-N-C under U = 0/−0.8 V for CO_2RR, and (b) structure diagrams (side and top views) related to the free-energy values of NC (left) and Nb-N-C (right) adsorbing *COOH. (c) Free-energies of NC and Nb-N-C under U = 0/1.23 V for ORR, and (d) structure diagrams associated to the free-energy values of NC and Nb-N-C adsorbing *O.

formation at the optimal potential of −0.8 V, which agrees with the outstanding FE_{CO} of NC and Nb-N-C catalysts. In terms of the rate-determining *COOH intermediate formation (Fig. 7b), the Nb-N-C exhibits a lower thermodynamic free energy (2.4 eV) than the NC catalyst (2.5 eV), confirming its preferable current density for CO_2RR activity.

Regarding the O_2-to-H_2O process, the uphill energy barrier of *O adsorbing on the Nb-N-C catalyst is lower than that of NC at an equilibrium potential of U = 1.23 V (Fig. 7c), facilitating the complete 4e⁻ transfer process of ORR for Nb-N-C. The thermodynamic free energy of *O on the Nb-N_4O site is 4.1 eV, which is much lower than the 4.5 eV for graphitic-N (Fig. 7d). The lower free energy of *O on Nb-N_4O benefits the subsequent *O desorption and hydrogenation processes, causing the preferable $E_{1/2}$ and E_{onset} values for the Nb-N-C catalyst towards ORR [90–95].

CONCLUSIONS

Niobium clusters/atoms anchored onto the NC matrix were primarily designed as bifunctional CO_2RR and ORR catalysts. Meanwhile, the homemade ZAB system was assembled with cathodic Nb-N-C for driving CO_2 electrolysis. Strikingly, (1) niobium clusters enabled the enhancement of the reductive current and achieved similar CO FE of NC (nearly 90%) for CO_2RR; (2) the Nb-N-C catalyst exhibited a preferable half-wave potential of 0.84 V *vs.* RHE and a maximum power density of 115.6 mW cm^{-2} for ZAB, superior to that of the NC substrate; (3) a ZAB-powered CO_2 electrolysis system converted CO_2 to CO with productivity ranging from 2.1 to 4.1 μmol h^{-1} mg_{cat}^{-1} during a 50-h reduction. Theoretical calculations were also performed to evaluate the catalytic mechanism of the Nb-N-C and NC catalysts, which revealed that the reduced energy barriers of intermediate formation were responsible for the potential-determining steps of the CO_2RR and ORR.

Received 9 July 2022; accepted 25 August 2022; published online 18 November 2022

1 Kim C, Dionigi F, Beermann V, *et al.* Alloy nanocatalysts for the electrochemical oxygen reduction (ORR) and the direct electrochemical carbon dioxide reduction reaction (CO_2RR). Adv Mater, 2019, 31: 1805617
2 Wan W, Liu X, Li H, *et al.* 3D carbon framework-supported CoNi nanoparticles as bifunctional oxygen electrocatalyst for rechargeable Zn-air batteries. Appl Catal B-Environ, 2019, 240: 193–200
3 Liu X, Yang H, He J, *et al.* Highly active, durable ultrathin $MoTe_2$ layers for the electroreduction of CO_2 to CH_4. Small, 2018, 14: 1704049
4 Yang M, Sun J, Qin Y, *et al.* Hollow CoFe-layered double hydroxide polyhedrons for highly efficient CO_2 electrolysis. Sci China Mater, 2021, 65: 536–542
5 Yang M, Liu Y, Sun J, *et al.* Integration of partially phosphatized bimetal centers into trifunctional catalyst for high-performance hydrogen production and flexible Zn-air battery. Sci China Mater, 2022, 65: 1176–1186
6 Peng X, Zhao S, Mi Y, *et al.* Trifunctional single-atomic Ru sites enable efficient overall water splitting and oxygen reduction in acidic media. Small, 2020, 16: 2002888
7 Xie J, Wang X, Lv J, *et al.* Reversible aqueous zinc-CO_2 batteries based on CO_2-HCOOH interconversion. Angew Chem Int Ed, 2018, 57: 16996–17001
8 Wang X, Xie J, Ghausi MA, *et al.* Rechargeable Zn-CO_2 electrochemical cells mimicking two-step photosynthesis. Adv Mater, 2019, 31: 1807807
9 Zheng W, Chen F, Zeng Q, *et al.* A universal principle to accurately synthesize atomically dispersed metal-N_4 sites for CO_2 electroreduction. Nano-Micro Lett, 2020, 12: 108
10 Liu S, Wang L, Yang H, *et al.* Nitrogen-doped carbon polyhedrons confined Fe-P nanocrystals as high-efficiency bifunctional catalysts for aqueous Zn-CO_2 batteries. Small, 2022, 18: 2104965
11 Liang G, Li X, Wang Y, *et al.* Building durable aqueous K-ion capacitors based on MXene family. Nano Res Energy, 2022, 1: e9120002
12 Mi Y, Qiu Y, Liu Y, *et al.* Cobalt-iron oxide nanosheets for high-efficiency solar-driven CO_2-H_2O coupling electrocatalytic reactions. Adv Funct Mater, 2020, 30: 2003438
13 Yang M, Liu S, Sun J, *et al.* Highly dispersed Bi clusters for efficient rechargeable Zn-CO_2 batteries. Appl Catal B-Environ, 2022, 307: 121145
14 Sharifi T, Gracia-Espino E, Chen A, *et al.* Oxygen reduction reactions on single- or few-atom discrete active sites for heterogeneous catalysis. Adv Energy Mater, 2019, 10: 1902084
15 Zhang X, Xue D, Jiang S, *et al.* Rational confinement engineering of MOF-derived carbon-based electrocatalysts toward CO_2 reduction and O_2 reduction reactions. InfoMat, 2022, 4: e12257
16 Xue X, Yang H, Yang T, *et al.* N,P-coordinated fullerene-like carbon nanostructures with dual active centers toward highly-efficient multifunctional electrocatalysis for CO_2RR, ORR and Zn-air battery. J Mater Chem A, 2019, 7: 15271–15277
17 Li R, Liu F, Zhang Y, *et al.* Nitrogen, sulfur co-doped hierarchically porous carbon as a metal-free electrocatalyst for oxygen reduction and carbon dioxide reduction reaction. ACS Appl Mater Interfaces, 2020, 12: 44578–44587
18 Li E, Yang F, Wu Z, *et al.* A bifunctional highly efficient FeN_x/C electrocatalyst. Small, 2018, 14: 1702827
19 Qi G, Zhao Q, Liu Q, *et al.* Biomass-derived carbon frameworks for oxygen and carbon dioxide electrochemical reduction. Ionics, 2021, 27: 3579–3586
20 Liu X, Zhou Y, Wang CL, *et al.* Solvent-free self-assembly synthesis of N-doped ordered mesoporous carbons as effective and bifunctional materials for CO_2 capture and oxygen reduction reaction. Chem Eng J, 2022, 427: 130878
21 Lü F, Zhao S, Guo R, *et al.* Nitrogen-coordinated single Fe sites for efficient electrocatalytic N_2 fixation in neutral media. Nano Energy, 2019, 61: 420–427
22 Zhang Y, Jiao L, Yang W, *et al.* Rational fabrication of low-coordinate single-atom Ni electrocatalysts by MOFs for highly selective CO_2 reduction. Angew Chem Int Ed, 2021, 60: 7607–7611
23 Sekhon SS, Park JS. Biomass-derived N-doped porous carbon nanosheets for energy technologies. Chem Eng J, 2021, 425: 129017
24 Jin M, Liu W, Sun J, *et al.* Highly dispersed Ag clusters for active and stable hydrogen peroxide production. Nano Res, 2022, 15: 5842–5847
25 Liu S, Jin M, Sun J, *et al.* Coordination environment engineering to boost electrocatalytic CO_2 reduction performance by introducing boron into single-Fe-atomic catalyst. Chem Eng J, 2022, 437: 135294
26 Chan MH, Fai Yeung C. Model-independent constraints on ultralight dark matter from the SPARC data. Astrophys J, 2021, 913: 25
27 Gao S, Liu Y, Xie Z, *et al.* Metal-free bifunctional ordered mesoporous carbon for reversible Zn-CO_2 batteries. Small Methods, 2021, 5: 2001039
28 Shen H, Gracia-Espino E, Ma J, *et al.* Synergistic effects between atomically dispersed Fe-N-C and C-S-C for the oxygen reduction reaction in acidic media. Angew Chem Int Ed, 2017, 56: 13800–13804
29 Chen M, Shao LL, Lv XW, *et al. In situ* growth of Ni-encapsulated and N-doped carbon nanotubes on N-doped ordered mesoporous carbon for high-efficiency triiodide reduction in dye-sensitized solar cells. Chem Eng J, 2020, 390: 124633
30 Li X, Wan K, Liu Q, *et al.* Nitrogen-doped ordered mesoporous carbon: Effect of carbon precursor on oxygen reduction reactions. Chin J Catal, 2016, 37: 1562–1567
31 Lü F, Bao H, Mi Y, *et al.* Electrochemical CO_2 reduction: From nanoclusters to single atom catalysts. Sustain Energy Fuels, 2020, 4: 1012–1028
32 Liu M, Lee J, Yang TC, *et al.* Synergies of Fe single atoms and clusters on N-doped carbon electrocatalyst for pH-universal oxygen reduction. Small Methods, 2021, 5: 2001165

33 Jiang Z, Wang T, Pei J, *et al.* Discovery of main group single Sb-N_4 active sites for CO_2 electroreduction to formate with high efficiency. Energy Environ Sci, 2020, 13: 2856–2863
34 Han L, Ren Z, Ou P, *et al.* Modulating single-atom palladium sites with copper for enhanced ambient ammonia electrosynthesis. Angew Chem Int Ed, 2021, 60: 345–350
35 Liu H, Fu J, Li H, *et al.* Single palladium site in ordered porous heteroatom-doped carbon for high-performance alkaline hydrogen oxidation. Appl Catal B-Environ, 2022, 306: 121029
36 Zhou L, Lu SY, Guo S. Recent progress on precious metal single atom materials for water splitting catalysis. SusMat, 2021, 1: 194–210
37 Mu Y, Wang T, Zhang J, *et al.* Single-atom catalysts: Advances and challenges in metal-support interactions for enhanced electrocatalysis. Electrochem Energy Rev, 2021, 5: 145–186
38 Jiang H, Xia J, Jiao L, *et al.* Ni single atoms anchored on N-doped carbon nanosheets as bifunctional electrocatalysts for urea-assisted rechargeable Zn-air batteries. Appl Catal B-Environ, 2022, 310: 121352
39 Chen Z, Su X, Ding J, *et al.* Boosting oxygen reduction reaction with Fe and Se dual-atom sites supported by nitrogen-doped porous carbon. Appl Catal B-Environ, 2022, 308: 121206
40 Qiao M, Wang Y, Wang Q, *et al.* Hierarchically ordered porous carbon with atomically dispersed FeN_4 for ultraefficient oxygen reduction reaction in proton-exchange membrane fuel cells. Angew Chem Int Ed, 2020, 59: 2688–2694
41 Xu J, Lai S, Qi D, *et al.* Atomic Fe-Zn dual-metal sites for high-efficiency pH-universal oxygen reduction catalysis. Nano Res, 2020, 14: 1374–1381
42 Zhao CX, Liu JN, Wang J, *et al.* Recent advances of noble-metal-free bifunctional oxygen reduction and evolution electrocatalysts. Chem Soc Rev, 2021, 50: 7745–7778
43 Zhang J, Chen Y, Liu Y, *et al.* Self-catalyzed growth of Zn/Co-N-C carbon nanotubes derived from metal-organic frameworks as efficient oxygen reduction catalysts for Zn-air battery. Sci China Mater, 2021, 65: 653–662
44 Dong F, Wu M, Chen Z, *et al.* Atomically dispersed transition metal-nitrogen-carbon bifunctional oxygen electrocatalysts for zinc-air batteries: Recent advances and future perspectives. Nano-Micro Lett, 2022, 14: 36
45 Chen Y, Ji S, Wang Y, *et al.* Isolated single iron atoms anchored on N-doped porous carbon as an efficient electrocatalyst for the oxygen reduction reaction. Angew Chem Int Ed, 2017, 56: 6937–6941
46 Qi D, Liu Y, Hu M, *et al.* Engineering atomic sites *via* adjacent dual-metal sub-nanoclusters for efficient oxygen reduction reaction and Zn-air battery. Small, 2020, 16: 2004855
47 Liu X, Zhai X, Sheng W, *et al.* Isolated single iron atoms anchored on a N, S-codoped hierarchically ordered porous carbon framework for highly efficient oxygen reduction. J Mater Chem A, 2021, 9: 10110–10119
48 Zhang Y, Wang X, Zheng S, *et al.* Hierarchical cross-linked carbon aerogels with transition metal-nitrogen sites for highly efficient industrial-level CO_2 electroreduction. Adv Funct Mater, 2021, 31: 2104377
49 Chen J, Wang T, Wang X, *et al.* Promoting electrochemical CO_2 reduction *via* boosting activation of adsorbed intermediates on iron single-atom catalyst. Adv Funct Mater, 2022, 32: 2110174
50 Wang R, Wang X, Weng W, *et al.* Proton/electron donors enhancing electrocatalytic activity of supported conjugated microporous polymers for CO_2 reduction. Angew Chem Int Ed, 2022, 61: e202115503
51 Zhang X, Guo J, Guan P, *et al.* Catalytically active single-atom niobium in graphitic layers. Nat Commun, 2013, 4: 1924
52 Tang H, Tian X, Luo J, *et al.* A Co-doped porous niobium nitride nanogrid as an effective oxygen reduction catalyst. J Mater Chem A, 2017, 5: 14278–14285
53 Fu J, Bao H, Liu Y, *et al.* Oxygen doping induced by nitrogen vacancies in Nb_4N_5 enables highly selective CO_2 reduction. Small, 2020, 16: 1905825
54 Song Y, Chen W, Zhao C, *et al.* Metal-free nitrogen-doped mesoporous carbon for electroreduction of CO_2 to ethanol. Angew Chem Int Ed, 2017, 56: 10840–10844
55 Shanmugapriya S, Zhu P, Yan C, *et al.* Multifunctional high-performance electrocatalytic properties of Nb_2O_5 incorporated carbon nanofibers as Pt support catalyst. Adv Mater Interfaces, 2019, 6: 1900565
56 Li B, Li Z, Wu X, *et al.* Interface functionalization in inverted perovskite solar cells: From material perspective. Nano Res Energy, 2022, 1: e9120011
57 Cui H, Zhu G, Liu X, *et al.* Niobium nitride Nb_4N_5 as a new high-performance electrode material for supercapacitors. Adv Sci, 2015, 2: 1500126
58 Tao H, Choi C, Ding LX, *et al.* Nitrogen fixation by Ru single-atom electrocatalytic reduction. Chem, 2019, 5: 204–214
59 Peng X, Mi Y, Bao H, *et al.* Ambient electrosynthesis of ammonia with efficient denitration. Nano Energy, 2020, 78: 105321
60 Li W, Amiinu IS, Zhang B, *et al.* Distorted niobium-self-doped graphene *in-situ* grown from 2D niobium carbide for catalyzing oxygen reduction. Carbon, 2018, 139: 1144–1151
61 Fu J, Cano ZP, Park MG, *et al.* Electrically rechargeable zinc-air batteries: Progress, challenges, and perspectives. Adv Mater, 2017, 29: 1604685
62 Lee S, Choi J, Kim M, *et al.* Material design and surface chemistry for advanced rechargeable zinc-air batteries. Chem Sci, 2022, 13: 6159–6180
63 Prakoso B, Mahbub MAA, Yilmaz M, *et al.* Recent progress in extending the cycle-life of secondary Zn-air batteries. ChemNanoMat, 2021, 7: 354–367
64 Tang C, Wang B, Wang HF, *et al.* Defect engineering toward atomic Co-N_x-C in hierarchical graphene for rechargeable flexible solid Zn-air batteries. Adv Mater, 2017, 29: 1703185
65 Liu X, He J, Zhao S, *et al.* Self-powered H_2 production with bifunctional hydrazine as sole consumable. Nat Commun, 2018, 9: 4365
66 Gao S, Jin M, Sun J, *et al.* Coralloid Au enables high-performance Zn-CO_2 battery and self-driven CO production. J Mater Chem A, 2021, 9: 21024–21031
67 Qi D, Lv F, Wei T, *et al.* High-efficiency electrocatalytic NO reduction to NH_3 by nanoporous VN. Nano Res Energy, 2022, 1: e9120022
68 Wang X, Liu S, Zhang H, *et al.* Polycrystalline SnS_x nanofilm enables CO_2 electroreduction to formate with high current density. Chem Commun, 2022, 58: 7654–7657
69 Meng G, Wei T, Liu W, *et al.* NiFe layered double hydroxide nanosheet array for high-efficiency electrocatalytic reduction of nitric oxide to ammonia. Chem Commun, 2022, 58: 8097–8100
70 Li L, Hasan IM, Qiao J, *et al.* Copper as a single metal atom based photo-, electro- and photoelectrochemical catalyst decorated on carbon nitride surface for efficient CO_2 reduction: A review. Nano Res Energy, 2022, 1: e9120015
71 Zhang L, Mao F, Zheng LR, *et al.* Tuning metal catalyst with metal-C_3N_4 interaction for efficient CO_2 electroreduction. ACS Catal, 2018, 8: 11035–11041
72 Chen J, Li Z, Wang X, *et al.* Promoting CO_2 electroreduction kinetics on atomically dispersed monovalent Zn^I sites by rationally engineering proton-feeding centers. Angew Chem Int Ed, 2022, 61: e202111683
73 Wang X, Feng S, Lu W, *et al.* A new strategy for accelerating dynamic proton transfer of electrochemical CO_2 reduction at high current densities. Adv Funct Mater, 2021, 31: 2104243
74 Zhang S, Chen M, Zhao X, *et al.* Advanced noncarbon materials as catalyst supports and non-noble electrocatalysts for fuel cells and metal-air batteries. Electrochem Energ Rev, 2021, 4: 336–381
75 Wang Y, Wang L, Fu H. Research progress of Fe-N-C catalysts for the electrocatalytic oxygen reduction reaction. Sci China Mater, 2022, 65: 1701–1722
76 Liang J, Liu Q, Alshehri AA, *et al.* Recent advances in nanostructured heterogeneous catalysts for N-cycle electrocatalysis. Nano Res Energy, 2022, 1: e9120010
77 Zhang H, Qiu Y, Zhang S, *et al.* Nitrogen-incorporated iron phosphosulfide nanosheets as efficient bifunctional electrocatalysts for energy-saving hydrogen evolution. Ionics, 2022, 28: 3927–3934
78 Ahmad T, Liu S, Sajid M, *et al.* Electrochemical CO_2 reduction to C_{2+} products using Cu-based electrocatalysts: A review. Nano Res Energy, 2022, 1: e9120021

79 Zhang Q, Zhang S, Luo Y, *et al.* Preparation of high entropy alloys and application to catalytical water electrolysis. APL Mater, 2022, 10: 070701
80 Hou J, Peng X, Sun J, *et al.* Accelerating hydrazine-assisted hydrogen production kinetics with Mn dopant modulated CoS_2 nanowire arrays. Inorg Chem Front, 2022, 9: 3047–3058
81 Zhang H, Luo Y, Chu PK, *et al.* Recent advances in non-noble metal-based bifunctional electrocatalysts for overall seawater splitting. J Alloys Compd, 2022, 922: 166113
82 Wei Z, Wang J, Guo S, *et al.* Towards highly salt-rejecting solar interfacial evaporation: Photothermal materials selection, structural designs, and energy management. Nano Res Energy, 2022, 1: e9120014
83 Meng L, Li L. Recent research progress on operational stability of metal oxide/sulfide photoanodes in photoelectrochemical cells. Nano Res Energy, 2022, 1: e9120020
84 Wan ST, Li HT, Ma ZH, *et al.* 2D/2D heterostructured MoS_2/$PtSe_2$ promoting charge separation in FTO thin film for efficient and stable photocatalytic hydrogen evolution. Rare Met, 2022, 41: 1735–1742
85 Pei Z. Symmetric is nonidentical: Operation history matters for Zn metal anode. Nano Res Energy, 2022, 1: e9120023
86 Zhou F, Zhou Y, Liu GG, *et al.* Recent advances in nanostructured electrocatalysts for hydrogen evolution reaction. Rare Met, 2021, 40: 3375–3405
87 Liu Y, Li W, Wu H, *et al.* Carbon dots enhance ruthenium nanoparticles for efficient hydrogen production in alkaline. Acta Phys-Chim Sin, 2021, 37: 2009082
88 Xu T, Liang J, Yue L, *et al.* Recent progress in metal-free electrocatalysts toward ambient N_2 reduction reaction. Acta Phys-Chim Sin, 2021, 37: 2009043
89 Han L, Ou P, Liu W, *et al.* Design of Ru-Ni diatomic sites for efficient alkaline hydrogen oxidation. Sci Adv, 2022, 8: eabm3779
90 Jiang L, Dong D, Lu YC. Design strategies for low temperature aqueous electrolytes. Nano Res Energy, 2022, 1: e9120003
91 Ye H, Li Y. Towards practical lean-electrolyte Li-S batteries: Highly solvating electrolytes or sparingly solvating electrolytes? Nano Res Energy, 2022, 1: e9120012
92 Gao S, Wei T, Sun J, *et al.* Atomically dispersed metal-based catalysts for Zn-CO_2 batteries. Small Struct, 2022, 2200086
93 Ge S, Zhang L, Hou J, *et al.* Cu_2O-derived PtCu nanoalloy toward energy-efficient hydrogen production *via* hydrazine electrolysis under large current density. ACS Appl Energy Mater, 2022, 5: 9487–9494
94 Dai Y, Xiong Y. Control of selectivity in organic synthesis *via* heterogeneous photocatalysis under visible light. Nano Res Energy, 2022, 1: e9120006
95 Huang W, Zhou D, Lee J, *et al.* Ag-decorated GaN for high-efficiency photoreduction of carbon dioxide into tunable syngas under visible light. Nanotechnology, 2021, 32: 505722

Acknowledgements This work was financially supported by the National Natural Science Foundation of China (22075211, 21601136, 22109118, 51971157, and 51621003).

Author contributions Gao S and Wang T conducted the experiment; Gao S designed this study, analyzed the data and wrote the paper; Jin M performed the theoretical calculation; Hu G did some characterizations. Yang H, Zhang S, Liu Q, Liu X and Luo J performed some data analysis and offered helpful suggestions. All authors contributed to the general discussion.

Conflict of interest The authors declare that they have no conflict of interest.

Supplementary information Supporting data are available in the online version of the paper.

Sanshuang Gao received his MS degree from the College of Materials Science and Engineering, Anhui University of Science and Technology, China, in 2018. His research interests mainly focus on the design, synthesis and applications of nanomaterials.

Guangzhi Hu received his PhD degree from the Chinese Academy of Sciences in 2010. After post-doctoral research at the Nano Carbon Materials Research Laboratory of the Department of Physics, Umeå University, Sweden, he joined the Chinese Academy of Sciences. Currently, he is a full-time professor at the Institute for Ecological Research and Pollution Control of Plateau Lakes, Yunnan University. His research interests focus on the application of functional nanomaterials in energy and environment.

Jun Luo received his BS (2001) and PhD (2006) degrees from Tsinghua University. Then, he worked as a postdoc at Warwick University and a research fellow at Oxford University. He joined Tsinghua University as an associate professor. In 2015, he moved to Tianjin University of Technology. Currently, He is a full professor at Shenzhen Institute for Advanced Study, University of Electronic Science and Technology of China. His research interests focus on low-dimensional materials and their electron microscopy.

Xijun Liu received his PhD degree from the College of Science, Beijing University of Chemical Technology in 2014. Then, he joined the School of Materials Science and Engineering, Tianjin University of Technology. Currently, he is a full-time professor at the School of Resource, Environments and Materials, Guangxi University. His current scientific interests focus on nanomaterials, heterogeneous catalysis, and materials design for catalysts and energy conversion/storage devices.

双功能Nb-N-C原子分散催化剂用于水系锌-空气电池驱动CO_2还原

高三双[1], 王天玮[1,2], 靳梦梦[1], 张书胜[3], 刘倩[4], 胡广志[5*], 杨慧[1], 罗俊[1,6*], 刘熙俊[2*]

摘要 设计廉价和高效的双功能催化剂应用于CO_2还原和O_2还原反应(CO_2RR和ORR)是实现碳中和的理想选择. 因此, 本文研制出铌原子分散固定在氮掺杂有序介孔碳(Nb-N-C)上的双功能CO_2RR和ORR催化剂用于锌-空气电池(ZAB)自驱动CO_2RR. 得益于高铌原子利用率和有序介孔结构, Nb-N-C催化剂展现出高达90%的CO法拉第效率, ORR的半波电位活性为0.84 V, ZAB的峰值功率活性为115.6 mW cm^{-2}. 此外, 采用两个串联的ZABs单元作为自供能CO_2RR系统的电源, 能够连续将CO_2转化为CO. 该自供能系统前10小时的CO平均产率为3.75 μmol h^{-1} mg_{cat}^{-1}. 理论计算表明, 铌原子分散固定在氮掺杂的碳上形成Nb–N配位键, 从而有效地降低CO_2RR的决速中间体*COOH和ORR的决速中间体*O的生成能垒.

